# Communication

# An Ultrawideband H-Plane Monopulse Log-Periodic Antenna for Jamming Signal Finding

Weihao Diao, Ruihong Li, Yue Li, and Zhijun Zhang

*Abstract*—**This communication proposes an ultrawideband (UWB) H-plane monopulse log-periodic antenna designed for UAV applications in jamming signal detection. The main radiators are two log-periodic dipole antennas (LPDAs). Good isolation between the two LPDA elements is achieved through the common mode (CM) and differential mode (DM) cancellation methods. The spacing factor of the LPDAs, and the distance between the elements are adjusted to improve DM matching and CM matching, with the radiation patterns also considered to ensure the detection distance, correctness, and accuracy of the direction-finding system. The balanced feeding network consists of a UWB monopulse comparator, parallel lines, and tapered microstrip lines. The proposed antenna operates in a band exceeding four octaves (1.45–5.95 GHz) for both the sum and differential ports, covering the GPS band (1.575 GHz) and Wi-Fi bands (2.4, 5 GHz). It exhibits low-ripple radiation patterns, a sum beam gain above 10.5 dBi, a null depth below – 20 dB, and a front-to-back ratio exceeding 14 dB.**

*Index Terms*—**Jamming signal direction finding, log-periodic antenna, monopulse antenna, ultrawideband (UWB), UWB decoupling.**

## I. Introduction

Nowadays, the reliability and security of the communication system become particularly important. In the face of growing spectrum congestion and complex electromagnetic environments, finding the source of jamming signals has become a key task.

Jamming signals can be in the GPS band (1.575 GHz), Wi-Fi band (2.4, 5 GHz), or other bands. Therefore, to detect jamming signals in a wide frequency range, an ultrawideband (UWB) antenna should be employed. There are two types of UWB antennas. One type is traveling wave antennas, such as horn antennas and Vivaldi antennas, and so on [1], [2], [3], [4], [5], and [6]. The other type is the antennas regulated into certain shapes to make different resonances occur at different locations, like magneto-electric antennas [7], log-periodic antennas [8], [9], and so on [10], [11], [12], and [13].

To find the direction of a jamming signal source, a monopulse antenna can be applied [14], [15], [16]. To identify azimuthal directions, a horizontally arrayed UWB monopulse antenna (UWBMA) is needed. Carrying the UWBMA by a UAV is an economical and simple option to accomplish the mission. As depicted in Fig. 1, to identify all the jamming signal sources in azimuthal directions, a UAV in the air only needs to rotate a round in the horizontal or azimuthal plane (the *xoy* plane) with its UWBMA working. Using an electronic scanning antenna for azimuthal direction-finding needs a combination of multiple antennas, increasing the complexity. Rotating a single port antenna for azimuthal direction-finding requires a very high gain or a very deep null for a good resolution, increasing the complexity and cost as well. Compared with the antennas mentioned above, a UAV carrying monopulse antenna has the advantages of being cost-effective and easy to achieve higher resolution. The polarization of the jamming signal is most likely to be vertical polarization (VP) due to its stable propagation characteristic, the lower loss of the ground reflection, and its common employment. Moreover, the wires or circuits in a UAV are usually horizontally configured, which will degrade the radiation patterns of horizontally polarized antennas [17]. For VP antennas, the horizontal plane is usually its H-plane, so the required UWBMA should be an H-plane array. Fig. 1(b) displayed an example of a VP H-plane log-periodic dipole antenna (LPDA) array, whose E-plane and H-plane are shown.

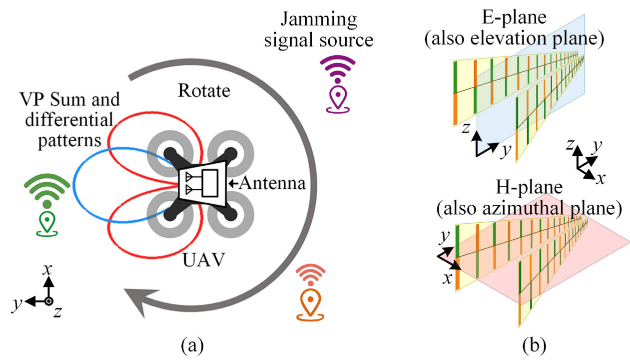


Fig. 1. (a) Schematic of finding the of jamming signals in azimuthal directions with a UAV. (b) E-plane and H-plane of an LPDA array.

Because of the azimuthal estimation, monopulse antennas must be arrayed in the horizontal plane. Thereby, E-plane arrayed antennas radiate horizontal polarization (HP) waves, and H-plane arrayed antennas radiate VP waves. There are some works designing UWBMAs. In [18] and [19], Vivaldi antennas are arrayed in the E-plane to form UWBMAs. The middle metal part of the antenna in [18] is shortened to reduce the sidelobe. Zhou et al. [20] utilizes two LPDAs to construct a UWB E-plane monopulse antenna. E-plane monopulse antennas are not adequate for VP jamming signal finding in azimuthal directions, and the antennas in [18], [19], and [20] occupy large areas, making it difficult to carry on a UAV. DuHamel et al. [21] designs a dual-polarized circular array of LPDAs to meet the requirements of polarization, but the feeding network behind the antenna is complicated and large in size. In [22], an H-plane log-periodic slot array is proposed. Although the polarization fits in, the heavy all-metal structure and large H-plane size of the slot array limit its application on UAVs.

When two Vivaldi antennas are arranged in the H-plane, undesired splitting of the differential beam occurs. Furthermore, the mutual coupling of H-plane arrayed two LPDAs is high because the antennas are in the strong field area of each other. The high mutual coupling

Manuscript received 22 February 2024; revised 11 June 2024; accepted 18 June 2024. Date of publication 28 June 2024; date of current version 9 September 2024. This work was supported in part by the National Natural Science Foundation of China under Contract 62271279. *(Corresponding author: Zhijun Zhang.)*

Weihao Diao, Yue Li, and Zhijun Zhang are with Beijing National Research Center for Information Science and Technology (BNRist), Tsinghua University, Beijing 100084, China (e-mail: zjzh@tsinghua.edu.cn).

Ruihong Li is with the National Engineering Research Center of Mobile Communication, Guangzhou 510310, China.

Color versions of one or more figures in this article are available at https://doi.org/10.1109/TAP.2024.3418208.

Digital Object Identifier 10.1109/TAP.2024.3418208

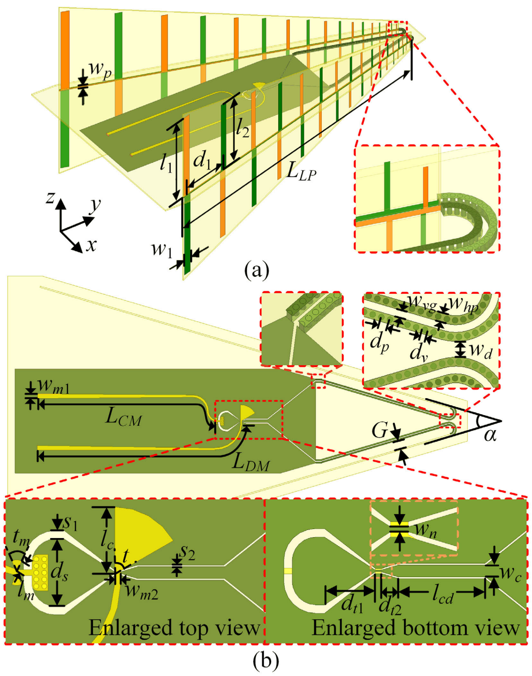


Fig. 2. Configuration of the proposed antenna. (a) Three-dimensional view. (b) Top view of the feeding network, and enlarged view of some details.

will cause bad matching of the sum and the differential ports of the monopulse antenna, degrading the system performance. So, designing an H-plane UWBMA is challenging.

In this communication, a UWB H-plane monopulse log-periodic antenna for jamming signal finding is proposed. The structure of this communication and the main contents in each section are introduced as follows. Section II presents the configuration of the proposed antenna. It is composed of two LPDAs, a UWB monopulse comparator and some transitions. In Section III, the design process of the proposed antenna is demonstrated. The mutual coupling between the two LPDAs is reduced by enlarging the spacing factor and decreasing the angle between the two LPDAs. A UWB monopulse comparator taking advantage of the (co-planar waveguide) CPW mode and the slot mode of slot lines is designed. For UWB matching, some transitions are introduced. Section IV demonstrates the results of the proposed antenna in simulation and measurement. The proposed antenna exhibits an impedance bandwidth (IBW) that surpasses four octaves (1.45–5.95 GHz), with the radiation patterns preserved in the whole band. In the working band, the peak gains of the sum beams and the differential beams are over 7.3 and 5.6 dBi, respectively. In Section V, a brief conclusion is made.

## II. Antenna Configuration

In this section, the structure and the optimized dimensions of the proposed antenna will be expounded. The configuration of the proposed UWBMA is shown in Fig. 2. In Fig. 2(a), three PCB boards are assembled: two with the LPDA printed on them and one with the feeding network printed on it. The substrate for all three boards is F4B, with a relative permittivity of 2.65 and a loss tangent of 0.0015. The LPDA boards have a thickness of 0.6 mm, while the feeding network board is 0.8 mm thick. The two LPDA boards are positioned at an angle of 32° to each other, denoted as $\alpha$ in Fig. 2(b), and they are perpendicular to the feeding network board.

The dimensions of a single 17-element LPAD arrayed in the proposed antenna are also depicted in Fig. 2(a). The metal layers on different planes of the board are represented in green and orange, respectively. The key two parameters of an LPDA are the scaling

TABLE I

Detailed Dimensions of the Proposed Antenna

| Para. | Value (mm) | Para. | Value (mm) | Para. | Value (mm) | Para. | Value (mm) | Para. | Value (mm) |
|---|---|---|---|---|---|---|---|---|---|
| $L_{LP}$ | 196.3 | $w_{m1}$ | 2.2 | $d_p$ | 0.6 | $s_2$ | 0.2 | $d_{t1}$ | 6 |
| $l_1$ | 55 | $L_{DM}$ | 100 | $d_v$ | 0.4 | $d_s$ | 8 | $d_{t2}$ | 2 |
| $l_2$ | 46.75 | $G$ | 4.2 | $w_{vg}$ | 0.5 | $t$* | 4 | $l_{cd}$ | 10.3 |
| $d_1$ | 32 | $l_c$ | 8 | $w_{hp}$ | 0.6 | $t_m$* | 45 | $w_c$ | 1.4 |
| $w_1$ | 5.2 | $l_m$ | 1.5 | $w_d$ | 1 | $w_{m2}$ | 0.7 | | |
| $w_p$ | 0.5 | $L_{CM}$ | 91.1 | $s_1$ | 1 | $w_n$ | 0.2 | | |

* The unit of the two parameters is °.

factor $\tau$ and the spacing factor $\sigma$, which are expressed as $\tau = l_{n+1}/l_n$, and $\sigma = d_n/(4l_n)$. Here, $l_n$ is the length of the $n$th longest dipole's arm on an LPDA and $d_n$ is the distance between the $n$th longest dipole and the (n − 1)th longest dipole on an LPDA. The dipoles on the LPDA are fed with parallel double strip lines and the two LPDAs are open-circuit at the terminal. The length and the width of the dipoles are both tapered. For simplicity, only the dimensions of the longest dipole and the second-longest dipole are given. Fig. 2(b) displays the top view of the proposed UWBMA together with the enlarged views of some details, where the UWB monopulse feeding network is shown. The enlarged top view and the enlarged bottom view of the UWB monopulse comparator are shown at the bottom of Fig. 2(b) in red dashed boxes, which are in the form of microstrip line and slot line [23], [24], [25], [26]. Tapered microstrip lines are utilized for impedance matching of the sum and differential ports. To feed the LPDAs with balanced current, horizontally placed parallel lines are used, which consist of double-side metal strips with dense metalized vias. The output ports of the comparator are connected with the horizontally placed parallel lines since the two types of lines are balanced. The enlarged 3-D view of a connecting part of the slot line and the parallel line is shown in the red dashed box at the top-left in Fig. 2(b). The proposed antenna is simulated and optimized with Ansys HFSS 2021. The optimized dimensions of the antenna are listed in Table I and the optimized scaling factor and spacing factor are $\tau = 0.85$ and $\sigma = 0.146$. The design process will be proposed in Section III.

## III. Antenna Design

This section will explain the design process and design considerations of the proposed antenna including the evolution of the H-plane two-element LPDA array and the design of the UWB monopulse comparator.

### A. H-Plane Two-Element LPDA Array

As is known, an LPDA can be divided into three regions: the transmission region, the active region, and the unexcited region [24]. The transmission region can be regarded as a segment of a capacitive-loaded transmission line and the active region is the main radiating part. The initial parameters of the LPDA are selected as $\tau = 0.85$ and $\sigma = 0.08$ since this is a common choice [28], [29], [30], [31]. The configuration of the initial two-element H-plane LPDA array is illustrated in Fig. 3(a) and (b). To achieve a distance of approximately a half wavelength between the two same-length dipoles on the two LPDAs, the parameters are set as $\alpha = 52°$ and $g = 12$ mm. The S parameters of the single LPDA and the initial array are shown in Fig. 3(c). It can be seen that both the single LPDA and the array are well-matched, but the mutual coupling of the array is high.

As is well-known, for a symmetric and reciprocal two-antenna system, the common mode (CM) and differential mode (DM) reflection coefficients are written as $S_{cc} = S_{11} + S_{21}$, $S_{dd} = S_{11} - S_{21}$. It can

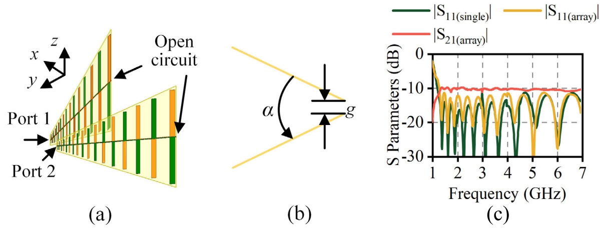


Fig. 3. (a) Three-dimensional view. (b) Top view of the initial H-plane two-element LPDA array. (c) S parameters of the single LPDA and the array.

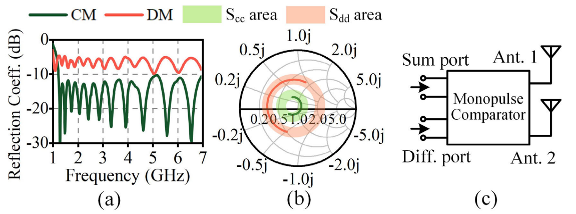


Fig. 4. Simulated CM and DM reflection coefficients of the initial array (a) in magnitude and (b) on the Smith chart. (c) Block diagram of a monopulse antenna.

be known that high mutual coupling will cause a mismatch of either CM or DM or both of them. The reflection coefficients of CM and DM are displayed in Fig. 4(a). It can be seen that the CM is matched while the DM is unmatched. The block diagram of a monopulse antenna is shown in Fig. 4(c). Apparently, the sum port matching and differential port matching are positively correlated to the CM and DM matching, respectively. Thereby, the impedance matching of the sum or antennas will be excited by the sum port while DM will be excited by the differential port. Back to the initial array, it can be concluded that the differential port matching is poor due to the bad DM matching. Bad matching causes not only the standing waves on the cables in the system, but also the deterioration of the LNA noise figure, resulting in signal fluctuation and drastic degradation of signal-to-noise ratio (SNR) [32]. It will further lead to the shrink of the detection distance of the direction-finding system. Thus, the mutual coupling should be suppressed. According to the CM and DM cancellation method [33], matching both CM and DM indicates the reduction of the mutual coupling. Therefore, by adjusting the CM and the DM impedances, the mutual coupling can be deceased so the sum and the differential ports of the monopulse system can be matched. In Fig. 4(b), $S_{cc}$ and $S_{dd}$ are plotted on the Smith chart. The trajectories of CM and DM reflection coefficients rotate around a center point in a circular pattern with varying frequency. For clarity, only the segments in the 3.2–3.5 GHz range are displayed in Fig. 4(b), with highlighted colored rings indicating the approximate areas occupied by the trajectories in the whole band (1.45–6 GHz). It can be observed that the radius of $S_{dd}$ is larger than that of $S_{cc}$. It means the bad DM matching and good CM matching corresponding to Fig. 4(a). Thus, the target of adjustment is to decrease the radii of $S_{cc}$ and $S_{dd}$.

The radiating environment has significant influences on the input impedance of an antenna. Hence, the field distributions of the array in CM and DM are investigated. In CM and DM analysis, one antenna in the system can be replaced by a PMC plane or PEC plane in the middle plane to simplify the analysis, as shown in Fig. 5. For the reason that the polarization of the LPDAs is parallel to the equivalent PMC or PEC plane, the field distributions of the two modes are dramatically different. In the CM case, the radiating environment of the LPDAs is favorable because the existence of the tangential $E$-field is allowed at the position of PMC. On the contrary, the PEC cannot support the tangential $E$-field on its surface. Consequently, the CM impedance is favorable while the DM impedance is less ideal.

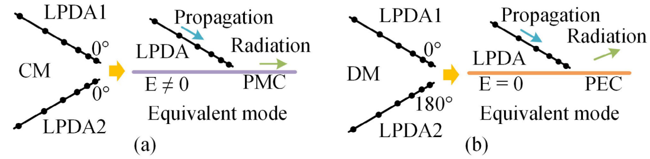


Fig. 5. Analysis of the H-plane two-element LPDA array in (a) DM and (b) CM.

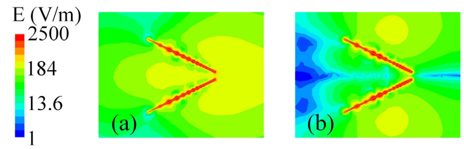


Fig. 6. Complex magnitude of the $E$-field distribution in the H-plane of (a) CM and (b) DM.

Moreover, the phase relationship between the dipoles in the active region can direct the radiating energy to propagate from the longer dipole to the shorter dipole. In other words, the propagating direction of the radiating wave (PDRW) on an LPDA is from the longer dipoles to the shorter dipoles. Due to the boundary condition, the PMC can guide the radiating wave of the LPDA in the tangential polarization along its tangential direction while PEC will reflect it as presented in Fig. 5. The complex magnitude of the $E$-field distribution in the H plane of CM and DM are illustrated in Fig. 6. It can be observed that the radiating wave of the two LPDAs is guided rightward in CM, while it is reflected by equivalent PEC in DM.

Based on the analysis above, the PDRW on the LPDAs and the distance between the corresponding active region (DBCAR) are the two critical factors affecting the input impedance of the DM. The DBCAR represents the distance between two same-length dipoles on the two LPDAs, serving as an indicator of the equivalent separation between the two LPDAs. The larger the DBCAR is or the closer the PDRW on the LPDAs is to the tangential direction, the lower the mutual coupling between the two LPDAs is. Note that the radiating environment of the CM is more akin to a single LPDA, making it less sensitive to changes in parameters. The evolution process of the H-plane two-element LPDA array and the results of the process are demonstrated in Figs. 7 and 8, respectively. Throughout the evolution, the distance before the two shortest dipoles is held constant at 12 mm while adjusting the spacing factor of the LPDAs and the angle between the LPDAs. First, the spacing factor of the LPDAs $\sigma$ is enlarged to increase the DBCAR without altering the PDRW, which is the transition from Case 1 to Case 2. The enlarged spacing factor significantly enhances the DM impedance matching, while causing a slight impact on the CM impedance. Consequently, $S_{dd}$ is reduced from about $-5$ dB to about – 14 dB, with the $S_{cc}$ almost unchanged, as shown in Fig. 8(b) and (e). Thus, the mutual coupling between the two LPDAs is reduced from $-10$ to $-15$ dB, as shown in Fig. 8(g). However, in Case 2, the DBCAR becomes excessively large, resulting in a high sidelobe and back lobe in the sum beam, which can cause the misjudgment of the jamming signal direction, as depicted in Fig. 8(c). It can be known that the DBCAR in Case 2 is close to one wavelength, an overly large distance for array elements. Because the configuration of the array assembles a horn facing left and the angle of 52° provides a more beneficial condition for backward wave propagation than the angle of 32°, the back lobe or front-to-back ratio (FBR) of Cases 1 and 2 is higher than Case 3. To mitigate the sidelobe and back lobe issue in the sum beam, the angle between the two LPDAs ($\alpha$) is decreased from 52° to 32°, representing the progression from Case 2 to Case 3. Note that the DBCAR in Case 3 is a little bit larger than that in Case 1. As seen in Fig. 8, the sidelobe, back lobe, and the mutual coupling are reduced. The FBR is improved from 12 to 18 dB. Although the DBCAR is decreased in Case 3, the PDRW on

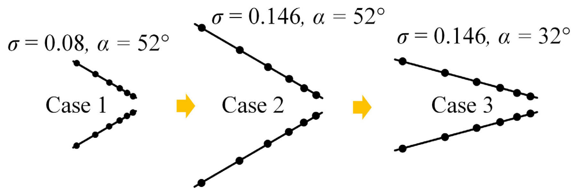


Fig. 7. Evolution process of the H-plane two-element LPDA array.

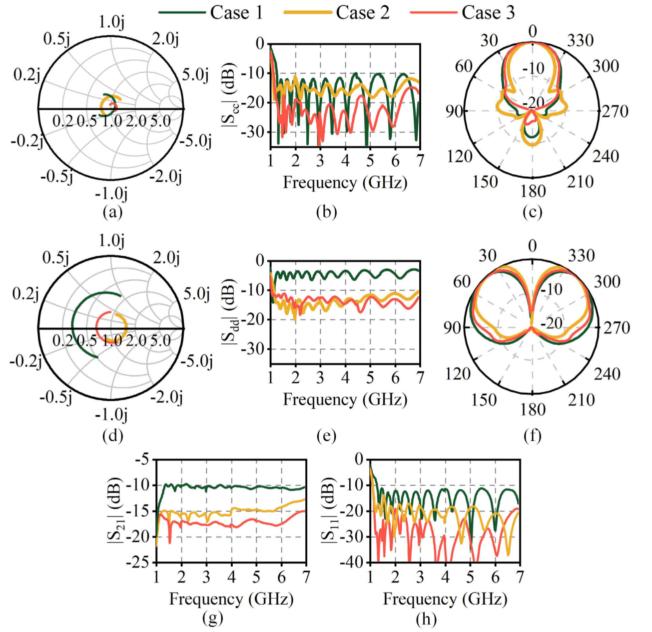


Fig. 8. Simulated (a) $S_{cc}$ and (d) $S_{dd}$ in 3.2–3.5 GHz in the Smith chart. The magnitude of (b) $S_{cc}$ and (e) $S_{dd}$. (c) Normalized sum beam. (f) Differential beam in the H-plane at 3.4 GHz (unit: dBi). (g) $S_{21}$ and (h) $S_{11}$ of the array in the evolution.

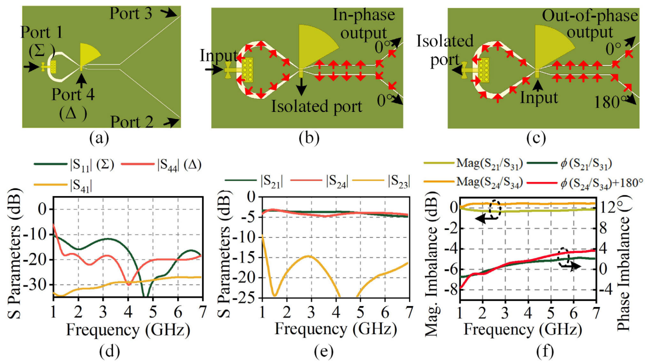


Fig. 9. (a) Geometry of the UWB monopulse comparator. Schematic of vector $E$-field distribution in the slot line of (b) CM (CPW mode) and (c) DM (slot mode). (d) and (e) Simulated S parameters. (f) Magnitude and phase imbalance of the comparator.

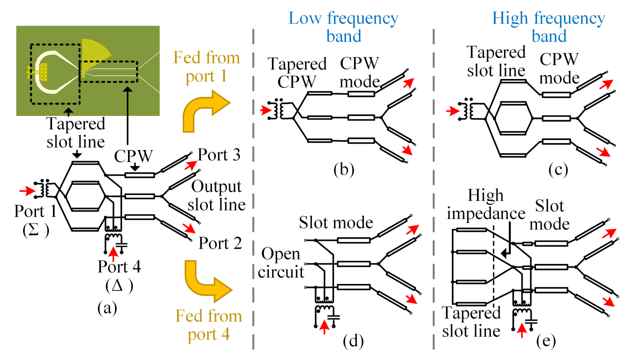


Fig. 10. (a) Equivalent circuit of the UWB monopulse comparator. Simplified circuit of the UWB comparator when fed from (b) and (c) sum port and (d) and (e) differential port.

the LPDAs is closer to the tangential direction of the equivalent PEC or PMC plane. It further improves the CM impedance matching with the DM impedance matching almost unchanged, thus reducing the mutual coupling, as shown in Fig. 8(b), (e), and (g). Besides, it can be observed that the impedance matching of either LPDA is improved in the process. Owing to the log-periodic configuration, the IBW and decoupling bandwidth can be broadened by increasing the number of dipoles on the LPDAs with other parameters unchanged. In the evolution, the mutual coupling is suppressed, and the matching of the CM and the DM are both improved, with the FBR increased. Thus, the matching of the sum and the differential ports, and the accuracy of the direction-finding system can be ensured.

### *B. UWB Monopulse Comparator*

The geometry and S parameters of the UWB monopulse comparator are shown in Fig. 9. The mode $E$-field distribution with different input port fed is shown in Fig. 9. The $E$-field is marked by red arrows. When fed from Port 1, the CPW mode is excited, where the $E$-field points from the middle metal to the side metal, as shown in Fig. 9(b). Thus, the outputs of Port 2 and 3 are in-phase and equal outputs are amplitude. When fed from Port 4, the slot mode is excited, thus, the anti-phase and equal amplitude, as shown in Fig. 9(c). Due to the orthogonality of the two modes, the two input ports are isolated. A bowtie-shaped shunt capacitor is added for the matching of Port 1. The S parameters of the UWB monopulse comparator are plotted in Fig. 9(d) and (e). It can be seen that the sum port and differential port are matched and isolated in the entire band, and the imbalances of the two output ports are low. As illustrated in Fig. 9(f), the imbalance between the two output ports is low.

The equivalent circuit of the UWB monopulse comparator is shown in Fig. 10(a). The UWB monopulse comparator can be divided into three parts: tapered slot line part, CPW part, and output slot line part. The correspondence between the equivalent circuit and the practical model is also shown in Fig. 10(a). The tapered slot line serves to provide a high impedance boundary for the differential port, which will be discussed later. The length of the CPW part can be adjusted for impedance tuning. The CPW width at the position of the differential port is narrowed to minimize the imbalance of the DM output, which rarely affects the impedance of the comparator. The output slot line part provides balanced outputs. When fed from the sum port, the CPW mode can be excited. The $E$-field at the differential port will be canceled out, so no energy goes to the differential port. The simplified circuits when fed from the sum port are depicted in Fig. 10(b) and (c). Under sum port feed at a low-frequency band, the tapered slot line can be regarded as tapered CPW, as shown in Fig. 10(b). When fed from the differential port, the slot mode can be excited. The $E$-field at the sum port will be canceled out, so the sum port is isolated from the differential port. The simplified circuits of the monopulse comparator fed from port 4 in different frequency bands are displayed in Fig. 10(d) and (e). It can be seen that the tapered slot line and the CPW are connected in parallel when fed from the differential port. In the low-frequency band, the middle metal of the tapered slot line part does not affect the $E$-field. Thus, the tapered slot line part is similar to a hole in the low-frequency band under differential port feed, which is equivalent to an open circuit as shown in Fig. 10(d). In the high-frequency band, the length of tapered slot lines is about a quarter wavelength, providing a high impedance boundary for the differential port, as shown in Fig. 10(e). Thereby, the energy fed from port 4 can be effectively guided rightward to the output ports with little reflection.

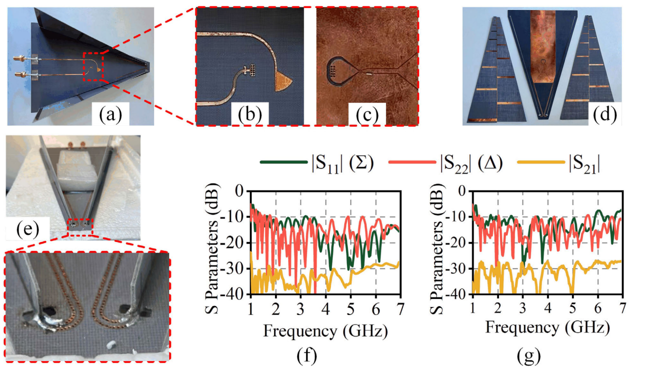


Fig. 11. (a) Three-dimensional view, (b) enlarged top view, (c) enlarged bottom view of the prototype, (d) three PCB boards, (e) feeding part of the two LPDAs, (f) simulated, and (g) measured S parameters of the prototype.

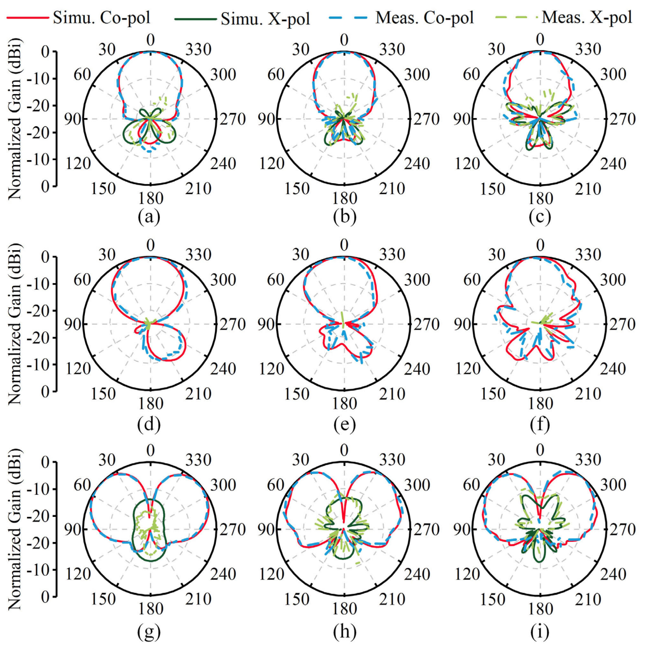


Fig. 12. Simulated and measured normalized radiation patterns of the proposed antenna. Sum patterns in H-plane at (a) 1.45 GHz, (b) 3.4 GHz, and (c) 5.95 GHz. Sum patterns in E-plane at (d) 1.45 GHz, (e) 3.4 GHz, and (f) 5.95 GHz. Differential patterns in the H plane at (g) 1.45 GHz, (h) 3.4 GHz, and (i) 5.95 GHz.

## IV. Experimental Verification

A prototype of the proposed antenna is fabricated as demonstrated in Fig. 11(a)–(e). Two coaxial cables are respectively used to feed the sum port and the differential port. The impedance characteristic of the fabricated prototype is measured with a vector network analyzer, and the radiation characteristic is measured in an anechoic chamber. The simulated and measured reflection coefficients and isolation are plotted in Fig. 11(f) and (g), revealing good agreement between simulation and measurement. The reflection coefficients remain lower than −10 dB in 1.45–5.95 GHz, and the isolation between the two ports is lower than −27 dB. Due to the potential inaccuracies caused by manual assembly, the measured reflection coefficient of the sum port exceeds −10 dB near 6 and 7 GHz. It is acceptable because the working band has already covered the desired band (1.575 GHz, 2.4 GHz, and 5.15 ~ 5.85 GHz). The simulated and measured normalized radiation patterns of the proposed antenna are illustrated in Fig. 12. It can be seen that the measurement coincides well with the simulation. As seen, there is little ripple in the radiation patterns, indicating the preservation of the sum beams and differential beams. The simulated and measured peak gain, null depth, and sum beam

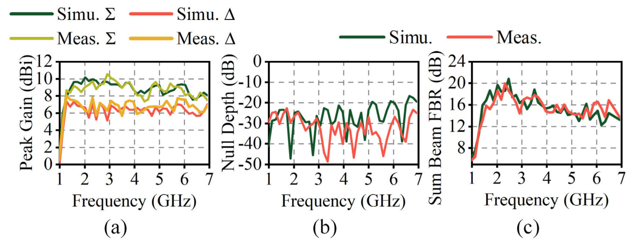


Fig. 13. Simulated and measured (a) gain, (b) null depths, and (c) sum beam's FBR of the proposed antenna.

TABLE II
Comparison Among the Proposed Work and Other Works

| Reference | Array type | IBW[1] ($f_{max}/f_{min}$) | Array plane size ($\lambda_m \times \lambda_m$)[2] | Maximal gain (dBi) |
|---|---|---|---|---|
| [18] | E plane | 3.42 | 1.03×1.55 | 14.2 |
| [19] | E plane | 3.45 | >1×1.5 | 8 |
| [20] | E plane | 2.20 | 1×2.67 | 10 |
| [21] | Circular | 6.00 | >0.6×1.2 | N.G.[4] |
| [22] | H plane | 1.32 | >1×0.66 | N.G. |
| This work | H plane | 4.10 | 0.61×1.04 | 10.5 |

[1] IBW is defined as the superposition of the sum and differential IBW.
[2] $\lambda_m$ is the wavelength at the lowest frequency in free space. The sizes not specified are measured based on photos in the references.

FBR are shown in Fig. 13. As shown, the peak gain of the sum beam consistently exceeds 7.3 dBi, and that of the differential beam is above 5.6 dBi through the entire band. The maximal gains of the sum beam and the differential beam are 10.5 and 7.7 dBi, respectively. The peak gain is stable in the working band because the tapering DBCAR makes the sizes of the radiation apertures at different frequencies similar. The null depth is below −20 dB and the sum beam FBR is above 14 dB in the working band.

Table II compares the proposed work and other works. The E plane arrayed antennas in [18], [19], and [20] are unsuitable for VP jamming signal finding in the azimuthal direction on account of their HP. Besides, the large footprint in the array plane makes it hard to be carried on UAVs. Both of the UWB dual-polarized monopulse antenna in [21] and the H-plane monopulse antenna in [22] can overcome the difficulty of polarization. Nevertheless, the complex feeding network behind the antenna in [21] significantly increases the overall size. In [22], the H-plane slot array occupies a large area and the all-metal design increases the weight. It should be mentioned that although the vertical size of the proposed antenna may be large, it is compatible with the design of a UAV.

## V. Conclusion

In this communication, a UWB H-plane monopulse log-periodic antenna for UAV application in jamming signal finding is proposed. CM and DM cancellation is applied to reduce the mutual coupling of the two-element H-plane LPDA array. The DM impedance is improved by enlarging the spacing factor of the LPDAs owing to the increase of the DBCAR. Then, the sidelobe attributed to the overlarge DBCAR is suppressed by decreasing the angle between the two LPDAs. The FBR is also improved due to the decrease of the angle. In the meantime, the CM impedance can be improved due to the change of the PDRW on the LPDAs. A UWB monopulse comparator in the form of microstrip lines and slot lines with horizontally placed parallel lines on the same PCB board is used to feed the two LPDAs. Limited to the processing technic, the input impedance of the comparator is 90 Ω, which is transformed to 50 Ω with the tapering microstrip line. The proposed antenna exhibits both the sum port and differential port IBW of more than four octaves (1.45–5.95 GHz).

The radiation patterns are preserved, and the FBR is improved in the whole band. The peak gains of the sum beam and differential beam are 7.3–10.5 dBi and 5.6–7.7 dBi in the entire band, respectively. The proposed antenna has great potential for jamming signal locating with UAVs for its wide matched working band, low null depth, good FBR, and low ripple of the radiation patterns.

## References


[1] R. Cicchetti, V. Cicchetti, A. Faraone, L. Foged, and O. Testa, "A wideband high-gain dielectric horn-lens antenna for wireless communications and UWB applications," *IEEE Trans. Antennas Propag.*, vol. 71, no. 2, pp. 1304–1318, Feb. 2023.

[2] E. G. Tianang, M. A. Elmansouri, and D. S. Filipovic, "Ultrawideband flush-mountable dual-polarized vivaldi antenna," *IEEE Trans. Antennas Propag.*, vol. 68, no. 7, pp. 5670–5674, Jul. 2020.

[3] J. Deng, R. Cao, D. Sun, Y. Zhang, and L. Guo, "Bandwidth enhancement of an Antipodal Vivaldi antenna facilitated by double-ridged substrate-integrated waveguide," *IEEE Trans. Antennas Propag.*, vol. 68, no. 12, pp. 8192–8196, Dec. 2020.

[4] Z.-Y. Zhang, K. W. Leung, and K. Lu, "Wideband high-gain omnidirectional biconical antenna for millimeter-wave applications," *IEEE Trans. Antennas Propag.*, vol. 71, no. 1, pp. 58–66, Jan. 2023.

[5] A. Liu and Y. Lu, "A superwide bandwidth low-profile monocone antenna with dielectric loading," *IEEE Trans. Antennas Propag.*, vol. 67, no. 6, pp. 4173–4177, Jun. 2019.

[6] O. Fiser et al., "UWB bowtie antenna for medical microwave imaging applications," *IEEE Trans. Antennas Propag.*, vol. 70, no. 7, pp. 5357–5372, Jul. 2022.

[7] C. Zhang, Y. Xie, Y. Wang, L. Dai, and L. Niu, "Novel miniaturized all-metal UWB magneto-electric monopole (MEM) antenna for multi-standard applications," *IEEE Trans. Antennas Propag.*, vol. 69, no. 7, pp. 4195–4200, Jul. 2021.

[8] K. Anim and Y.-B. Jung, "Shortened log-periodic dipole antenna using printed dual-band dipole elements," *IEEE Trans. Antennas Propag.*, vol. 66, no. 12, pp. 6762–6771, Dec. 2018.

[9] Q. Chen, Z. Hu, Z. Shen, and W. Wu, "2–18 GHz conformal low-profile log-periodic array on a cylindrical conductor," *IEEE Trans. Antennas Propag.*, vol. 66, no. 2, pp. 729–736, Feb. 2018.

[10] L. Sang, J. Xu, Z. Liu, Y. Mei, W. Wang, and Z. Shen, "Low-RCS UWB planar monopole array antenna based on the optimized design of the conductor layers," *IEEE Trans. Antennas Propag.*, vol. 71, no. 4, pp. 3683–3688, Apr. 2023.

[11] L. Y. Nie, X. Q. Lin, Z. Q. Yang, J. Zhang, and B. Wang, "Structure-shared planar UWB MIMO antenna with high isolation for mobile platform," *IEEE Trans. Antennas Propag.*, vol. 67, no. 4, pp. 2735–2738, Apr. 2019.

[12] Y. Zhang and Y. Li, "Wideband microstrip antenna in small volume without using fundamental mode," *Electromagn. Sci.*, vol. 1, no. 2, pp. 1–6, Jun. 2023.

[13] M. Shirazi, T. Li, J. Huang, and X. Gong, "A reconfigurable dual-polarization slot-ring antenna element with wide bandwidth for array applications," *IEEE Trans. Antennas Propag.*, vol. 66, no. 11, pp. 5943–5954, Nov. 2018.

[14] Y. J. Cheng, W. Hong, and K. Wu, "Design of a monopulse antenna using a dual V-type linearly tapered slot antenna (DVLTSA)," *IEEE Trans. Antennas Propag.*, vol. 56, no. 9, pp. 2903–2909, Sep. 2008.

[15] Y. Gao, W. Jiang, W. Hu, Q. Wang, W. Zhang, and S. Gong, "A dual-polarized 2-D monopulse antenna array for conical conformal applications," *IEEE Trans. Antennas Propag.*, vol. 69, no. 9, pp. 5479–5488, Sep. 2021.

[16] J. Zhu, S. Liao, S. Li, and Q. Xue, "60 GHz substrate-integrated waveguide-based monopulse slot antenna arrays," *IEEE Trans. Antennas Propag.*, vol. 66, no. 9, pp. 4860–4865, Sep. 2018.

[17] Y. Zhang, Y. Li, W. Zhang, Z. Zhang, and Z. Feng, "Omnidirectional antenna diversity system for high-speed onboard communication," *Engineering*, vol. 11, pp. 72–79, Apr. 2022.

[18] Y.-W. Wang, G.-M. Wang, Z.-W. Yu, J.-G. Liang, and X.-J. Gao, "Ultra-wideband $E$-plane monopulse antenna using Vivaldi antenna," *IEEE Trans. Antennas Propag.*, vol. 62, no. 10, pp. 4961–4969, Oct. 2014.

[19] G. Adamiuk, W. Wiesbeck, and T. Zwick, "Multi-mode antenna feed for ultra wideband technology," in *Proc. IEEE Radio Wireless Symp.*, Jan. 2009, pp. 578–581.

[20] H. Zhou, N. A. Sutton, and D. S. Filipovic, "W-band endfire log periodic dipole array," in *Proc. IEEE Int. Symp. Antennas Propag. (APSURSI)*, Jul. 2011, pp. 1233–1236.

[21] R. DuHamel, M. Armstrong, and W. Pedler, "Dual-polarization monopulse antennas utilizing conical arrays of log-periodic antennas," in *Proc. Antennas Propag. Soc. Int. Symp.*, vol. 4, Dec. 1966, pp. 159–166.

[22] M. Lu, E. Michielssen, P. Mayes, and P. Ingerson, "A dual mode log-periodic cavity-backed slot array," in *Proc. IEEE Antennas Propag. Soc. Int. Symp. Dig. Held Conjunct., USNC/URSI Nat. Radio Sci. Meeting*, vol. 1, Jul. 1999, pp. 124–127.

[23] M. Aikawa and H. Ogawa, "A new MIC magic-T using coupled slot lines," *IEEE Trans. Microw. Theory Techn.*, vol. MTT-28, no. 6, pp. 523–528, Jun. 1980.

[24] Y. Li, Z. Zhang, W. Chen, Z. Feng, and M. F. Iskander, "A dual-polarization slot antenna using a compact CPW feeding structure," *IEEE Antennas Wireless Propag. Lett.*, vol. 9, pp. 191–194, 2010.

[25] Y. Li, Z. Zhang, Z. Feng, and M. F. Iskander, "Dual-mode loop antenna with compact feed for polarization diversity," *IEEE Antennas Wireless Propag. Lett.*, vol. 10, pp. 95–98, 2011.

[26] Y. Li, Z. Zhang, J. Zheng, and Z. Feng, "Dual-polarised monopole-slot co-located MIMO antenna for small-volume terminals," *Electron. Lett.*, vol. 47, no. 23, pp. 1259–1260, 2011.

[27] R. Carrel, "Analysis and design of the log-periodic dipole antenna," Ph.D. dissertation, Dept. Elect. Eng., Univ. Illinois, Champaign, IL, USA, 1961.

[28] D. E. Anagnostou, J. Papapolymerou, M. M. Tentzeris, and C. G. Christodoulou, "A printed log-periodic koch-dipole array (LPKDA)," *IEEE Antennas Wireless Propag. Lett.*, vol. 7, pp. 456–460, 2008.

[29] X. Gao, Z. Shen, and C. Hua, "Conformal VHF log-periodic balloon antenna," *IEEE Trans. Antennas Propag.*, vol. 63, no. 6, pp. 2756–2761, Jun. 2015.

[30] Z. Hu, Z. Shen, W. Wu, and J. Lu, "Low-profile log-periodic monopole array," *IEEE Trans. Antennas Propag.*, vol. 63, no. 12, pp. 5484–5491, Dec. 2015.

[31] R. Wakabayashi, K. Shimada, H. Kawakami, and G. Sato, "Circularly polarized log-periodic dipole antenna for EMI measurements," *IEEE Trans. Electromagn. Compat.*, vol. 41, no. 2, pp. 93–99, May 1999.

[32] D. M. Pozar, *Microwave Engineering*, 3rd ed. Hoboken, NJ, USA: Wiley, 2005, pp. 512–514.

[33] L. Sun, Y. Li, Z. Zhang, and H. Wang, "Antenna decoupling by common and differential modes cancellation," *IEEE Trans. Antennas Propag.*, vol. 69, no. 2, pp. 672–682, Feb. 2021.